



## Towards microwave imaging of cells†

Cite this: *Lab Chip*, 2018, 18, 463

Mehmet Kelleci,‡<sup>a</sup> Hande Aydogmus,‡<sup>a</sup> Levent Aslanbas,‡<sup>a</sup>  
Selcuk Oguz Erbil,‡<sup>a</sup> and M. Selim Hanay <sup>\*ab</sup>

Received 23rd November 2017,  
Accepted 4th December 2017

DOI: 10.1039/c7lc01251a

rsc.li/loc

Integrated detection techniques that can characterize the morphological properties of cells are needed for the widespread use of lab-on-a-chip technology. Herein, we establish a theoretical and experimental framework to use resonant microwave sensors in their higher order modes so that the morphological properties of analytes inside a microfluidic channel can be obtained electronically. We built a phase-locked loop system that can track the first two modes of a microstrip line resonator to detect the size and location of microdroplets and cells passing through embedded microfluidic channels. The attained resolution, expressed in terms of Allan deviation at the response time, is as small as  $2 \times 10^{-8}$  for both modes. Additionally, simulations were performed to show that sensing with higher order modes can yield the geometrical volume, effective permittivity, two-dimensional extent, and the orientation of analytes. The framework presented here makes it possible to develop a novel type of microscope that operates at the microwave band, *i.e.*, a radar for cells.

## Introduction

Microfluidics holds immense potential for developing low-cost, compact, and disposable devices. Progress in this field has been enabled by innovations in soft lithography,<sup>1,2</sup> on-chip integration,<sup>3</sup> and microdroplet manipulation<sup>4</sup> technologies. Although microfluidic chips have small form factors, optical microscopy is usually required when working with microfluidic systems, *e.g.*, for obtaining the morphological properties of the cells that are being studied. Unfortunately, such reliance on optical microscopy has been one of the major roadblocks<sup>5–9</sup> limiting the widespread use of microfluidic devices because of size, portability, and cost issues.

Therefore, it is vitally important to develop new detection and imaging techniques that are compact and low-cost, yet rich in sensory data. In this regard, electronic sensing techniques offer inherent advantages in terms of cost and integrability.<sup>10,11</sup> Microwave resonant sensors, in particular, possess some unique properties since electromagnetic sensing is not limited by Debye screening at microwave frequencies.<sup>12</sup> Microwave sensors can be fabricated conveniently and their resonance frequencies can be tracked very accurately. In addition, these sensors are sufficiently sensitive to detect individ-

ual cells,<sup>13</sup> and their cost can be lowered substantially by using customized components.<sup>14</sup>

To date, experiments with resonant microwave sensors have focused on detecting capacitive changes, which yields the electrical properties of the analytes. Herein, we show that the morphological properties of analytes, in addition to their electrical properties, can be extracted from the very same sensors if a latent resource is utilized, *i.e.*, the higher-order modes of a microwave resonant sensor. Little attention has been paid to the use of higher-order modes in the context of microwave sensors in microfluidics; in contrast, such techniques have advanced the capabilities of micro- and nano-mechanical sensors substantially. For instance, multimode mechanical sensors have been used to locate microparticles,<sup>15</sup> weigh single molecules in real time,<sup>16</sup> measure the mass and stiffness of analytes simultaneously,<sup>17</sup> weigh neutral nanoparticles,<sup>18</sup> decouple the effects of multiple particles on the same sensor,<sup>19</sup> and obtain spatial information to form an inertial image.<sup>20</sup> These accomplishments have been enabled by multimode techniques in the mechanical domain, but there have been no counterparts in the domain of electromagnetic sensors.

Herein, we demonstrate how multimode sensing can be implemented with electromagnetic sensors operating in the microwave band.

Microwave sensors can detect analytes passing through a nearby microfluidic channel (Fig. 1). As an analyte enters the measurement region, it induces frequency shifts in all modes, and the shift in each mode depends on the spatial overlap between the shape of the analyte and the eigenvector of the particular mode (*i.e.* the mode shape). If frequency shifts from

<sup>a</sup> Department of Mechanical Engineering, Bilkent University, Ankara, 06800 Turkey. E-mail: selimhanay@bilkent.edu.tr

<sup>b</sup> National Nanotechnology Research Center (UNAM), Bilkent University, Ankara, 06800 Turkey

† Electronic supplementary information (ESI) available. See DOI: 10.1039/c7lc01251a

‡ These authors contributed equally to this work.

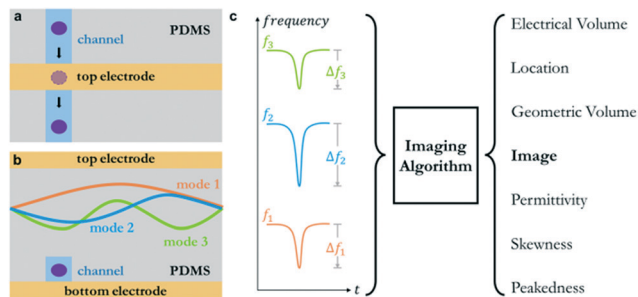


**Fig. 1** Multimode microwave sensing: panel (a) shows the top view and panel (b) shows the side view of the device paradigm. The first three mode-shapes are shown as the difference in the voltages between the two electrodes; (c) as each analyte passes through the sensing region, it induces frequency shifts on all modes. By using these shifts, the morphological and dielectric properties of the analytes can be obtained electronically.

multiple modes can be measured, then the locations, sizes, and shapes of analytes can be obtained by using the framework presented in this paper. Once this information becomes available, global shape features can be extracted readily, such as geometric or Zernike moments. Then, these global features can be used for cell classification tasks<sup>21,22</sup> and to construct quantitative images of analytes.<sup>20,23</sup>

Microwave resonators can be used as effective sensors<sup>24</sup> for concentration<sup>25,26</sup> and particle detection.<sup>27,28</sup> These sensors are usually characterized with a network analyzer where the frequency and the linewidth of the resonance can be monitored. To obtain narrower linewidths, active feedback mechanisms<sup>29</sup> can be used to improve sensitivity.<sup>30,31</sup> In our system, a network analyzer is not used except for the initial characterization; rather, a dedicated system was constructed to track the resonance frequencies of the first two-modes simultaneously and in real-time (Fig. 2). This system is composed of two digitally-controlled signal generators and two lock-in amplifiers. Each half of the circuit is a microwave interferometer.<sup>13</sup> With this circuitry, we simultaneously tracked the first two modes of a microstrip line resonator by using two parallel phase-locked loop (PLL) circuits in real-time. Typical frequencies of sensors used in the experiments

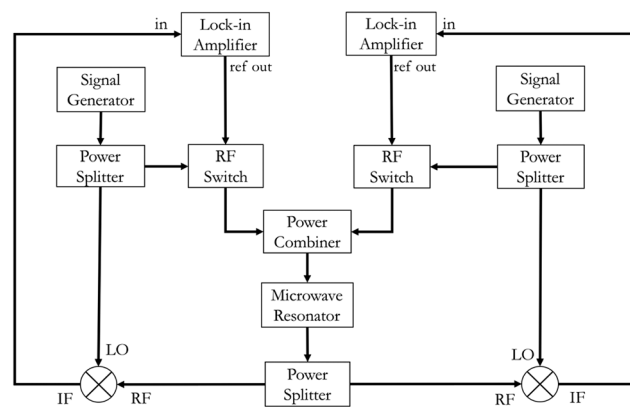


**Fig. 2** Electronic measurement setup for the simultaneous tracking of two resonance modes of a microwave sensor.

(when the microfluidic channels are filled with DI water) are 1.49 GHz for the first mode and 2.97 GHz for the second mode, whereas the quality factors are 54 and 48 for the first and second modes, respectively.

The microstrip line resonator extends over and probes several microfluidics channels (Fig. 3). As the microdroplets passed through the different channels, we measured the induced frequency shifts in both modes.

These frequency shifts were used to calculate the location of each droplet as well as its electrical volume (defined as the volume integral of the permittivity distribution). Later, two-mode sensors were used to detect individual HeLa and MDA-MB-157 cells and obtain the size spectra of the samples.

To simulate four-mode measurements, finite element method (FEM) analyses were performed, which enabled the determination of the geometric volume and effective permittivity of the analytes. With the framework presented here, it is possible to obtain all-electronic images of the analytes at microwave frequencies.

## Results and discussion

In dielectric impedance sensing,<sup>31,32</sup> a small particle passing through a channel modulates the effective permittivity of the resonator and induces a shift in the resonance frequency of the mode:<sup>33</sup>

$$\frac{\Delta f_n}{f_n} = - \frac{\int_{V_0} \Delta \epsilon(\mathbf{r}) E_n^2(\mathbf{r}) d^3 \mathbf{r}}{\int_{V_0} (\epsilon(\mathbf{r}) E_n^2 + \mu(\mathbf{r}) H_n^2) d^3 \mathbf{r}}$$

where  $f_n$  is the original resonance frequency of the mode,  $\Delta f_n$  is the change in the resonance frequency (*i.e.*, the signal used for sensing),  $\epsilon$  is the dielectric constant of the medium,  $\mu$  is the permeability of the medium,  $E_n$  is the electrical field,  $H_n$  is the magnetic field for the  $n$ th mode, and  $\Delta \epsilon$  is the change in the dielectric constant of the region occupied by the particle as calculated by the Maxwell Garnett approach. If the permittivities of the host medium and the particle are close to each other, then  $\Delta \epsilon \approx \epsilon_{\text{particle}} - \epsilon_{\text{host}}$  as expected; however, if

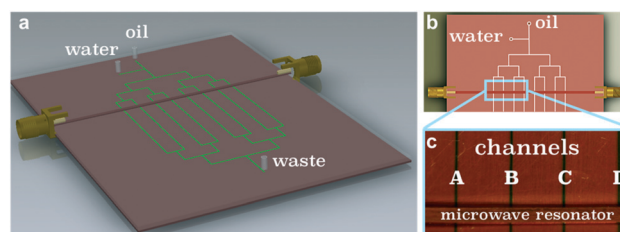


**Fig. 3** Microfluidic device used in the experiment: (a) 3D schematics of the microfluidics/microwave device; (b) schematic diagram of the microfluidic channels (white), the microwave resonator in the form of a microstrip line (dark orange), and the ground plane (light orange) with SMA connectors (yellow) on both ends; (c) micrograph of the device showing the region where the four microfluidic channels carrying droplets pass under the microwave strip line resonator.

the permittivity values are significantly different, then the Clausius–Mossotti factor can be used for full accuracy.

We defined the left-hand side of the equation above as the fractional frequency shift  $\left(\delta f_n \equiv \frac{\Delta f_n}{f_n}\right)$ . Also, we noted that the denominator of the right-hand side of the equation is the total energy stored in the resonator,  $E_{\text{res}}$ , and used the harmonic oscillator property  $\left(\langle \int \epsilon E_n^2 d^3\mathbf{r} \rangle = \langle \int \mu H_n^2 d^3\mathbf{r} \rangle\right)$  at resonance. Then, the equation can be written as:

$$\delta f_n = -\frac{\int_{V_0} \Delta\epsilon(\mathbf{r})\phi_n^2(\mathbf{r})d^3\mathbf{r}}{2V_n} \quad (1)$$

where  $V_n$  is the effective electrical volume of the mode:  $V_n = \int_{V_0} \epsilon(\mathbf{r})\phi_n^2 d^3\mathbf{r}$ . In the expression, the overall strength of the electrical field ( $E_n$ ) drops out.

Using this equation as a starting point, the spatial properties of the permittivity distribution function of a particle ( $\Delta\epsilon(\mathbf{r})$ ) can be probed. To demonstrate how information about  $\Delta\epsilon(\mathbf{r})$  can be extracted in a model platform, we fabricated a microstrip line resonator with microfluidic channels buried underneath (Fig. 3). Microstrip line resonators are used commonly as microwave sensors because they can be fabricated with a planar process. The microstrip line resonator in the experiments was electrically shorted on both sides and has a total length of 69 mm. In the experiments, the first two modes of the microstrip line were tracked continuously.

The microfluidic portion of the device was fabricated using soft lithography. Two input ports (water/oil) were used to generate water microdroplets in a continuous flow of oil (Fig. 3). These water microdroplets are used in the experiments for size and position determination. The length of the generated microdroplets was about 200  $\mu\text{m}$  as observed using a stereomicroscope equipped with a digital camera. The channels surrounding the microdroplets had a cross-section of 200  $\mu\text{m}$  by 75  $\mu\text{m}$ . These droplets then traveled toward and passed underneath the microstrip line resonator, which extends between the two SMA ports (Fig. 3). During the passage of the microdroplets, the microfluidic system branched into four channels. At each branching point, the droplets flowed into one of the two possible channels almost randomly (as determined by channel resistances and the passage of earlier droplets). In this way, an ensemble of droplets was generated that passed through all four channels with similar probabilities. Each channel crossed the signal path of the resonator at different locations, so that the utility of multimode sensing for position determination can be tested. At any given time, at most one channel carried a microdroplet through the active region of the microwave sensor. To keep the mode shapes as symmetrical as possible, another set of four channels was fabricated at the other half of the resonator, but this set was not used for droplet passage experiments. Details of the fabrication of the device are provided in the Methods section.

## Point-particle approximation and the determination of position

For a point particle, we can write  $\Delta\epsilon(\mathbf{r}) = v\delta(\mathbf{r} - \mathbf{r}_p)$ , where  $\mathbf{r}_p$  is the position of the particle,  $\delta$  is the Dirac delta function, and  $v$  is the total excess electrical volume of the particle. We can consider a one-dimensional microstrip line (Fig. 1) as a generic electromagnetic resonator to probe the positions of the particle along the axial direction. Then, the frequency shifts in the first two modes read as follows:

$$\delta f_1 = -\frac{v}{2V_1}\phi_1(x)^2 \quad (2)$$

$$\delta f_2 = -\frac{v}{2V_2}\phi_2(x)^2 \quad (3)$$

For a given platform, the electrical volume of the modes ( $V_n$ ) can be calculated, thereby leaving two unknowns for the problem ( $v, x$ ) and two equations. If the electromagnetic resonator is designed such that  $(\phi_1(x)/\phi_2(x))^2$  is an invertible function,<sup>16</sup> then these equations can be solved, and the position of the particle can be determined.

Considering the device shown in Fig. 3, in which the microfluidic channels flow directly below the signal path of the microstrip line, the droplets passing through different channels will generate different frequency shifts in both modes. The frequency shift for each mode is proportional to the square of the local electric field ( $E_n^2(\mathbf{r})$ ) for that mode, as shown in eqn (2) and (3) above. The electric field only has a  $z$ -component directly underneath the microstrip line, so fringing fields can be neglected in the active region, *i.e.*,  $\mathbf{E}(\mathbf{r}) = E(\mathbf{r})\hat{\mathbf{k}}$ . The electric field will have only a slight variation in the  $y$ - and  $z$ -directions because the microfluidic channel has a minuscule cross-sectional area. In this case, we can express the  $n$ th mode of the electric field as:

$$\mathbf{E}_n(\mathbf{r}) = A_n\phi_n(x)\hat{\mathbf{k}}$$

where  $A_n$  is the modal amplitude, and  $\phi_n(x)$  is the mode shape function for the resonator. For a microstrip line terminated with shorts at both ends, this function can be expressed as:

$$\phi_n(x) = \sin(\pi nx)$$

where the spatial coordinate of  $x$  is normalized with respect to the length of the microstrip line,  $L$ . The frequency shift caused by a particle with an excess dielectric volume ( $v$ ) can be calculated as:

$$\delta f_n = -\frac{v}{2V_n}\sin^2(\pi nx)$$

By using the first two modes and restricting the analysis to the first half of the sensor ( $0 < x < 0.5$ ), we obtain:

$$x = \frac{1}{\pi} \arccos \left( \sqrt{\frac{\delta f_2}{4\delta f_1}} \right) \quad (4)$$

After the location is known, then the (excess) electrical volume of the analyte also can be determined by using position information,  $x$ , in either modal eqn (2) or (3). One of the hallmarks of two-mode detection is that, when the frequency shift data points are scattered on the two-dimensional plane defined by  $\delta f_1$  and  $\delta f_2$ , each position contour (*i.e.*, the curve on which the value of  $x$  is constant) is a straight line that passes through the origin. The slope of this line changes for different position values, as was shown earlier using single-molecule nanomechanical sensors.<sup>16</sup> To track the resonance frequencies of the microwave sensor, a PLL circuit was used for each mode (Fig. 4(a)). In the PLL circuit, the output frequency of a voltage-controlled oscillator (VCO) is updated using the phase response of the microwave sensor. The phase of the microwave resonator is adjusted to  $0^\circ$  at resonance, and any deviation from the  $0^\circ$  phase produces an error signal that is used in a proportional-integrative (PI) feedback loop to update the frequency of the VCO. In this way, the VCO tracks the resonance frequency of the microwave sensor.

To track two resonance modes simultaneously, two PLLs were multiplexed using standard microwave components (Fig. 2). First, we used water microdroplets that were generated in an oil flow as analytes. As each analyte passed under the microstrip line, it caused clearly visible frequency shifts in both modes as detected by our measurement circuitry (Fig. 4(b)).

The data for the two-mode frequency shift can be represented in the 2D plane formed by the frequency shifts for

both modes (Fig. 5). As shown in eqn (4), the ratio between the frequency shift of the second mode to that of the first mode determines the location of the droplet. This means that the contours for the position in the 2D frequency-shift plane consist of lines that pass through the origin<sup>16</sup> (Fig. 5, inset).

Remarkably, the scatter plots for the shifts in the experimental frequency clearly show four distinct bands, with each one corresponding to a different channel through which droplets can pass; the channels are labeled A, B, C, and D in the scatter plot in Fig. 5, in the image of the device in Fig. 3c, and in the PLL data shown in Fig. 4b.

Independent measurements of the same droplets with a microscope confirmed that the classification based on the frequency shifts agreed with the actual paths of the droplets. Using a single electronic line, we successfully assigned the channel for each droplet. More importantly, position measurements – the first step for spatial resolution – were accomplished with a two-mode technique.

The 2D scatter plot provides information about the locations of the droplets and about their sizes. The size of each analyte can be quantified using the excess electrical volume, which is defined as the geometrical volume of the analyte multiplied by the difference between the dielectric constants of the analyte and the medium. The contours for a constant electrical volume are shown in the inset of Fig. 5, as well. The experimental data in the scatter plot indicate that the droplets were close in size, as expected. To obtain a more quantitative spectrum, the data can be projected into electrical volume and position dimensions. The resulting histogram (Fig. 6a) for electrical volume indicates a sharp peak, reflecting the almost monodisperse nature of the droplets produced in the system. This sharp histogram is also significant because the resonant measurements at different locations can be combined to yield the same value for the electrical volume. In addition, the histogram for the droplet

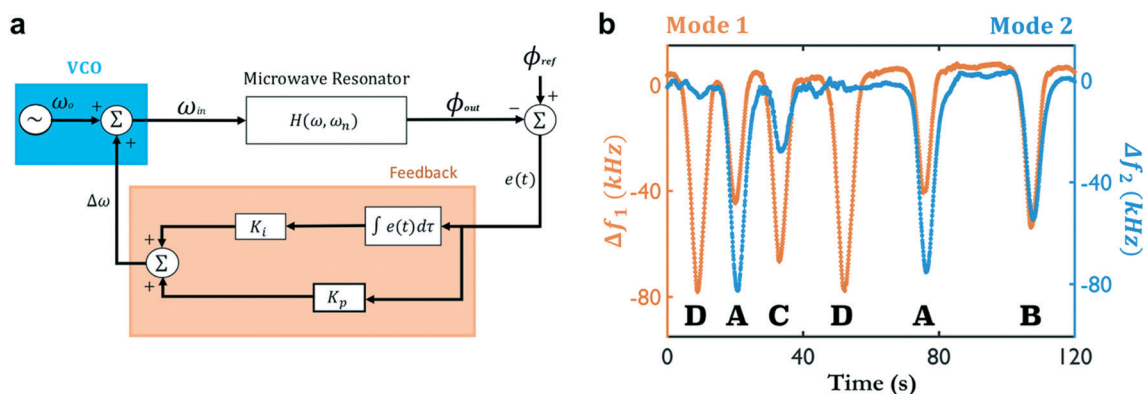


**Fig. 4** (a) Measurement system for each mode used is based on phase-locked loops. A voltage controlled oscillator (VCO) excites the microwave resonator, which produces a phase shift  $\phi_{out}$  at the output. When the phase of the resonator deviates from the reference phase  $\phi_{ref}$ , the resulting error signal,  $e$ , is used by the integrative ( $K_i$ ) and proportional ( $K_p$ ) feedback systems to produce a correction signal,  $\Delta\omega$ , to keep the VCO frequency at the microwave resonator frequency. (b) Two-mode frequency shifts due to droplet passage measured by two parallel PLLs; the orange trace shows the first mode, and the blue trace shows the second mode. The offset frequencies of  $f_1 = 1.4245$  GHz and  $f_2 = 2.88701$  GHz are subtracted for clarity. Depending on the channel (A, B, C or D) of the droplet, the ratio between the frequency shifts change; for instance, droplets passing through channel D, which is near the center of the strip line, induce almost no frequency shift in the second mode since it has a node at the center of the resonator.

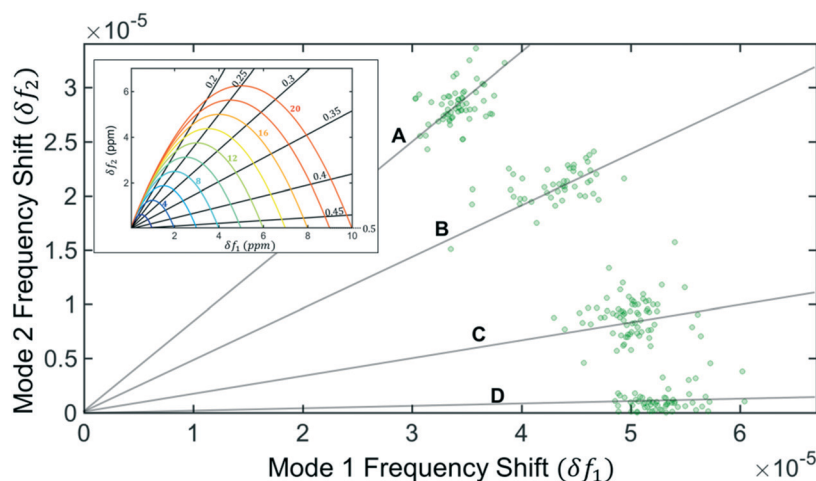


Fig. 5 Microdroplet data represented in the two-mode frequency shift domain. Overlapping events are shown by a change in color. The inset shows the straight contour lines for position (normalized to unity, so 0.5 means the center of the beam). The contours for electrical volume are shown as circular-shaped curves (expressed in ppm of the electrical volume of the device).

positions also can be obtained (Fig. 6b). The resulting positions in the histogram agree with the actual locations of the channels in the device within the  $2\sigma$  error level. As is evident from the figure, the classification of the droplet channels clearly was accomplished, and position information was obtained electronically.

After the two-mode technique was established, the same sensors were used to measure HeLa and MDA-MB-157 cell lines. The electrical volumes of both cell lines are much smaller than those of the microdroplets measured earlier. Despite the large difference in electrical volumes, the multimode microwave sensors successfully detected the passage of individual HeLa and MDA-MB-157 cells in a physiological buffer (Fig. 7a and b). Two-mode measurements increased the confidence levels for detecting the cells since both modes respond simultaneously. By using the two-mode frequency shifts, electrical volume histograms for the ensemble of HeLa and MDA-MB-157 cells were obtained (Fig. 7c).

The resulting histogram for the HeLa cells indicated that their electrical size was about two orders of magnitude smaller than the microdroplets that we measured before. For

the HeLa cell line, the excess electrical volume of individual cells is measured to be  $15.2 \times 10^{-7}$  ( $\sigma = 8.4 \times 10^{-7}$ ) whereas the electrical volume for individual MDA-MB-157 cells is measured to be  $1.97 \times 10^{-6}$  ( $\sigma = 8.4 \times 10^{-7}$ ). This indicates an (excess) electrical volume ratio of 2.6 or (excess) size ratio of 1.4. Previously, the presence of a microdroplet in a channel increased the fluidic resistance of the channel significantly and caused an almost equal distribution of the droplets into the channels. This dynamic effect is insignificant for the case of cells which are much smaller than the dimensions of the channel. Thus, it was observed through independent microscopy studies that most of the cells followed the path(s) of least resistance. The position histogram of both cells also supported this conclusion, even though the resolution of the position in this case was degraded due to the lower signal-to-noise ratio for single cell measurements, as expected. To demonstrate positional sensitivity at the single-cell level, we took advantage of the complementary set of channels fabricated on the same device. The input/output ports can be configured to activate the set of channels in either half of the device. In this way, the channels that exhibit the least resistance to the flow of cells can be modified. With this modification, a clear difference between the positional information for each cell lines have emerged (ESI,† section 9). The results represented in the frequency plane or in the position histograms show a clear distinction between the central channel where MDA cells pass and peripheral channels where HeLa cells pass. These results show that label-free cytometry and size-based characterization of cells are possible.

We performed FEM simulations and additional experiments using PCBs with drilled holes and a different microfluidic device (ESI,† sections 1–3). All of the results indicated that the aforementioned formula could be used to correctly calculate the positions of the particles. The location of the particles and the detection of the electrical volume are substantial advancements, *i.e.*, the location of a particle throughout a microfluidic channel can be determined without a

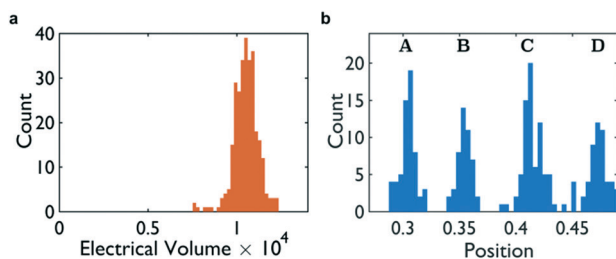


Fig. 6 (a) Histogram for the electrical volume of the microdroplets (normalized to the electrical volume of the sensor). (b) Position histogram (normalized to the length of the sensor) of the microdroplets. The center of the electrical volume corresponds to a volume of water that is  $\sim 60 \mu\text{m}$  in diameter. In the position histogram, events in which the second mode response is below the noise limit are excluded from consideration for clarity.

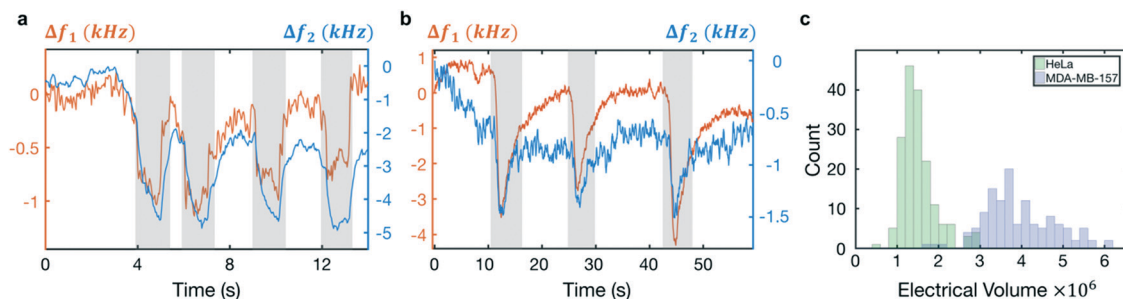


Fig. 7 Measurements on HeLa and MDA-MB-157 cells: two mode PLL data showing the entrance and exit of (a) single HeLa and (b) single MDA-MB-157 cells into the active sensing region; (c) the electrical volume for the HeLa and MDA-MB-157 cell lines each showed a dominantly mono-dispersed size population.

microscope or multiplexed sensor arrays. By using only one electrical signal line and two modes, we were able to infer the location of the particle in real time. In this manner, the trajectory and speed of a particle also can be determined in real-time along the channel. With one-mode sensing, the trajectory of a particle can be determined only after the particle has passed through the middle point, where the maximal value of the frequency shift is used as an indicator. With capacitive sensing, the location of the particle can be determined when the particle is in close proximity with the capacitive electrode. With the two-mode technique, however, the location of the particle is known at any moment. Therefore, accurate position and velocity measurements in applications, such as transit time<sup>34</sup> experiments or the real-time feedback control of particle locations,<sup>35</sup> can be accomplished without a microscope-based imaging system. More importantly, this work represents the first demonstration of microfluidic microwave sensors with inherent position sensitivity through the device.

### Sizing analytes and determining the relative permittivity

When the dimensions of the particle are significant compared to the length of the resonator, the point-particle assumption becomes less accurate and the integral eqn (1) should be used. To measure the characteristics of the analyte, multiple modes need to be used. In this case, the electrical and spatial parameters of the analytes can be obtained using the corresponding equation for each of the modes that are being tracked. The information from different modes can be used if a suitable linear transformation can be formed, as was shown for mechanical systems before.<sup>20</sup> By using the frequency shifts calculated above, relevant electrical and spatial information can be obtained. In this case, information is extracted as the expected value of a selected target function,  $g(\mathbf{r})$ . We can merge frequency shifts ( $\delta f_n$ ) from different modes by forming a special weighted superposition:<sup>20</sup>

$$\underbrace{\sum_{n=1}^{n=N} \alpha_n \delta f_n}_{\text{weighted superposition}} = -\frac{1}{\Omega_{\text{res}}} \int_{V_0} \Delta \varepsilon(\mathbf{r}) \times \underbrace{\left[ \sum_{n=1}^{n=N} \alpha_n \phi_n^2(\mathbf{r}) \right]}_{\substack{=g(\mathbf{r}) \\ \text{target function}}} \times d^3 \mathbf{r} \quad (5)$$

By using an algorithm to determine the optimal values for  $\alpha_n$ ,<sup>20</sup> we can obtain the expected value of the target function  $g(\mathbf{r})$ , which can be picked so that it is a spatial parameter of the analyte:

$$-\sum_{n=1}^{n=N} \alpha_n \delta f_n = \frac{1}{\Omega_{\text{res}}} \int_{V_0} \Delta \varepsilon(\mathbf{r}) g(\mathbf{r}) d^3 \mathbf{r} = \langle g(\mathbf{r}) \rangle$$

For instance, if the  $\alpha_n$  values are selected in such a way that the target function  $g(\mathbf{r})$  is equal to the unity function, then the total dielectric volume of the particle can be obtained:

$$-\sum_{n=1}^{n=N} \alpha_n \delta f_n = \frac{1}{\Omega_{\text{res}}} \int_{V_0} \Delta \varepsilon(\mathbf{r}) \underbrace{g(\mathbf{r})}_{1} d^3 \mathbf{r} = \frac{1}{\Omega_{\text{res}}} \int_{V_0} \Delta \varepsilon(\mathbf{r}) d^3 \mathbf{r} = \frac{\Omega_{\text{particle}}}{\Omega_{\text{res}}}$$

Therefore, the electrical volume of the particle can be calculated as:

$$\Omega_{\text{particle}} = \Omega_{\text{res}} \times \sum_{n=1}^{n=N} \alpha_n \delta f_n \quad (6)$$

where the quantities on the right-hand side are known. They can either be calculated using Maxwell's equations ( $\Omega_{\text{res}}$ , the electrical volume of the resonator), measured in the experiments ( $\delta f_n$ , frequency shift of each mode), or adjusted by the user through an algorithm detailed below and in the literature<sup>20</sup> ( $\alpha_n$ , weight coefficients).

After the electrical volume,  $\Omega_{\text{particle}}$ , is obtained, it can be used to normalize the permittivity distribution,  $\Delta \varepsilon(\mathbf{r})$ , so that the normalized quantity works as the probability density function (pdf) or particle size distribution (psd) of the particle:

$$\text{pdf}(\mathbf{r}) = \frac{\Delta \varepsilon(\mathbf{r})}{\Omega_{\text{particle}}}$$

A different selection of coefficients,  $\beta_n$ , will generate a different target function; for instance, picking  $g(\mathbf{r}) = x$  and normalizing the entire expression with  $\Omega_{\text{res}}$  will yield the mean position of the particle  $\langle x \rangle$ :

$$\begin{aligned} \frac{-1}{\Omega_{\text{res}}} \sum_{n=1}^N \beta_n \delta f_n &= \frac{1}{\Omega_{\text{res}}} \int_{V_0} \Delta \varepsilon(\mathbf{r}) \underbrace{g(\mathbf{r})}_{x} d^3 \mathbf{r} \\ &= \frac{\Omega_{\text{particle}}}{\Omega_{\text{res}}} \int_{V_0} \text{pdf}(\mathbf{r}) x d^3 \mathbf{r} = \frac{\Omega_{\text{particle}}}{\Omega_{\text{res}}} \langle x \rangle \end{aligned}$$

To obtain a proxy for the size of the particle, the standard deviation and the variance of the electrical volume can be used by constructing the superposition  $g(\mathbf{r}) = (x - \langle x \rangle)^2$ . Note that the value of the position is obtained by using the same set of measured frequency shifts,  $\delta f_n$ ; we are merely changing how the superposition is formed by changing  $\alpha_n$  weights. In this way, higher order moments also can be calculated. This is not a free resource however; if  $N$  modes are measured, then  $N$  pieces of independent information (*e.g.*, the first  $N$  moments or, alternatively,  $N$  Legendre moments of particle's shape) can be obtained.

To obtain the target function  $g(\mathbf{r})$ , there is an optimal (thus unique) choice for the  $\alpha_n$  coefficients, which is:<sup>20</sup>

$$\alpha_n = T_{mn}^{-1} b_m \quad (7)$$

where  $T_{mn}$  is the overlap integral between the responsivities of the modes, *i.e.*:

$$T_{mn} = \int_{\Omega} E_n^2(\mathbf{r}) E_m^2(\mathbf{r}) d^3 \mathbf{r} \quad (8)$$

and  $b_m$  is the overlap integral between the responsivity and the target function, *i.e.*:

$$b_m = \int_{\Omega} g(\mathbf{r}) E_m^2(\mathbf{r}) d^3 \mathbf{r} \quad (9)$$

By evaluating these overlap integrals, one can choose suitable  $\alpha_n$  coefficients to construct a superposition integral that can be used to calculate a specific moment of the particle's shape.

### Moments to imaging

After an adequate number of moments have been acquired, this information is used to reconstruct the shape, *i.e.*, the image of the analyte. Regular moments of the distribution can be used to reverse calculate the distribution (*i.e.*, shape) of the analyte through the Hausdorff procedure<sup>36,37</sup> or maximum entropy image reconstruction.<sup>38,39</sup>

To demonstrate the calculation of the geometric size (as opposed to the electrical volume, which depends on the electrical permittivity of the analyte), we performed Monte Carlo simulations in MATLAB, where the location, size, and permittivity of the particles were assigned randomly. The frequency shifts in the first four modes of a microwave resonator were generated using eqn (1), and then they were processed *via* the selection of appropriate values of weights using the approach described above. The electrical volume, location, and variance of the particle were calculated. Then, the variance values were converted into sizes

by assuming that the particle had a uniform, prismatic shape. An ensemble of 100 Monte Carlo particles was generated and analyzed in this way. In most of the cases, the measured values (through the inertial imaging algorithm) overlapped with the actual values. The first 15 particles of the ensemble are illustrated in Fig. 8a. After the geometric size was determined, it was combined with the electrical volume measurements to obtain the effective permittivity of the particle. For the Monte Carlo simulations, the actual and calculated permittivity values for the particles are shown in Fig. 8b. Detailed statistics for the performance of the algorithm are presented in the Methods section. The higher-order modes of the microwave resonator can be incorporated with the same technique<sup>20</sup> to obtain the higher-order moments and, eventually, the image of an analyte. Additional Monte Carlo simulations were performed to obtain the 2D size, length, width, and orientation of rectangular particles using 2D resonators (Fig. 8c). In this case, the first sixteen modes of a 2D electromagnetic resonator were used. The 2D resonator is modelled as a cavity resonator with a 1.5:1 aspect ratio along the  $x$ - $y$  directions used for sensing. In the simulations, all four edges along the resonator are shorted to the ground. The results (Fig. 8d) showed that the 2D algorithm can determine these values successfully including the orientation of the particle with respect to the resonator.

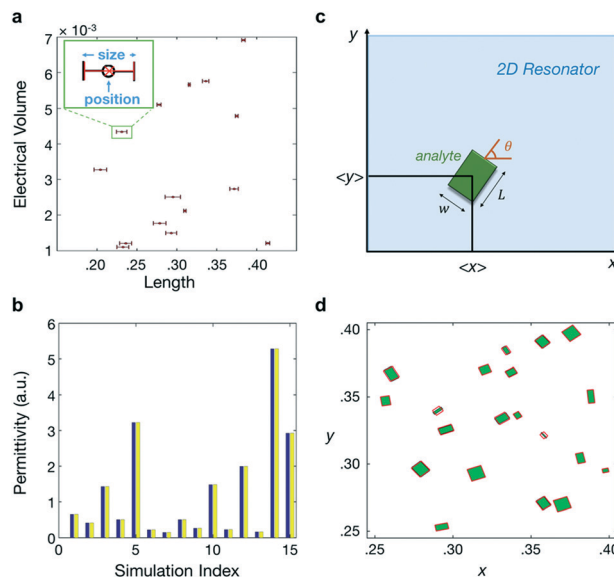


**Fig. 8** Size, permittivity and orientation determination using higher-order modes: (a) electrical volume, position, and size for the simulated (measured) particles are shown in black (red). (b) By dividing the electrical volume of the particle by the geometrical size, the effective permittivity of each particle used in the Monte Carlo simulations was determined correctly; the blue bars show the simulated values, and the yellow bars show the calculated results; (c) two-dimensional imaging model with a particle of dimensions ( $L, w$ ) and orientation angle  $\theta$  with respect to the resonator; (d) Monte Carlo simulation results showing actual (green) and calculated (red) shapes of the particles using 2D microwave sensors.

## Noise analysis

As is evident from the simulation results, spatial properties significantly less than the wavelengths of the modes can be extracted, since the multimode superposition technique is not limited by diffraction effects. In the experiments which required a large dynamic range, spatial resolution usually was limited by the frequency noise. Different PLL parameters are used for the droplet and cell sensing. For the larger microdroplet experiments, the PLL parameters chosen allowed for an Allan deviation of  $5 \times 10^{-7}$ , whereas  $2 \times 10^{-8}$  for both modes were obtained during the cell measurements for PLL response times of approximately 400 ms (ESI† section 8).

The uncertainty in measured parameters such as electrical volume and position is determined by the frequency noise in the experiments. Detailed noise analyses are provided in the supplementary information of ref. 16 and 20. Here we provide a simplified analysis that relates the positional uncertainty to frequency noise of the modes used. Eqn (4) shows the functional relationship between position ( $x$ ) and the frequency shifts ( $\delta f_1$ ,  $\delta f_2$ ) which we rewrite in the simplified form  $x = g(\delta f_1, \delta f_2)$ . Using the formula that relates the variance of multiple random variables to their functions, we can write:

$$\sigma_x^2 = \left[ \frac{\partial g}{\partial \delta f_1} \right]_{\delta f_1, \delta f_2}^2 \sigma_1^2 + \left[ \frac{\partial g}{\partial \delta f_2} \right]_{\delta f_1, \delta f_2}^2 \sigma_2^2 + 2 \left[ \frac{\partial g}{\partial \delta f_1} \frac{\partial g}{\partial \delta f_2} \right]_{\delta f_1, \delta f_2} \rho \sigma_1 \sigma_2$$

In the equations  $\sigma_1$  and  $\sigma_2$  show the Allan deviation of the first and second modes and  $\rho$  shows the correlation coefficient between the two modes ( $-1 < \rho < 1$ ). By using the measured Allan deviations ( $5 \times 10^{-7}$  for droplet detection experiments) and eqn (4), we can calculate the variance and standard deviation in each position measurement. The mean value for the position measurements yields  $\langle \sigma_x \rangle = 0.0056$  in the normalized length. Since the length of the resonator is about 69 mm, two-sigma corresponds to 0.77 mm.

On the other hand, we can calculate the noise statistics of the measured  $x$  values directly from the histogram. For each channel, the standard deviation of  $x$  is measured and a mean value is obtained by calculating the weighted-average. The standard deviation for the position measured in this way is  $\langle \sigma_x \rangle = 0.0086$ , reasonably close to the value calculated by using the frequency noise. The two-sigma positional uncertainty calculated in this way is 1.15 mm.

## Methods

### Device fabrication

All of the microfluidic devices reported in this manuscript are fabricated with the same procedure. The first step is to prepare the microchannel mold; SU-8 is spin coated on a 4 inch silicon wafer. As an adhesive layer, spin coated HMDS is used. The microchannel pattern is transferred to SU-8 *via* photolithography. After development, exposed parts of SU-8 are left on the wafer, forming an open mold with the chan-

nel pattern embossed on the surface of the wafer. Later, PDMS is mixed with a curing agent with a mass ratio of 10 to 1 and the air bubbles are removed from the mixture using a low pressure chamber, forcing the air bubbles to burst. A clean PDMS mixture is poured onto the mold inside a Petri dish and air bubbles are once again purged before placing it in an oven, preheated to 80 °C. After 1 hour, the mold is taken out of the oven and cooled down to room temperature in approximately 10 minutes. PDMS is cut in a rectangular shape and gently peeled off and microfluidic port holes are punched out wherever necessary.

The PDMS layer has microchannel features etched on one side and is plasma bonded on another flat surface in order to form microchannels. A copper plate with 500  $\mu\text{m}$  thickness is cut into a rectangle with desired dimensions, polished and coated with a thin layer of the PDMS mixture. It is kept inside the oven for  $\sim 24$  hours at 80 °C. After it is cooled down to room temperature, it is placed inside an oxygen plasma chamber alongside the microchannel carrying PDMS. After 40 seconds, surfaces exposed to the plasma are activated. The microchannel carrying surface is carefully aligned with the PDMS coated copper plate and stuck together by hand. Afterwards, a copper microstrip is fabricated out of the same copper plate with 500  $\mu\text{m}$  thickness. The copper plate is carefully sliced with guillotine shears, forming a rectangular cable with constant width along its length. The microstrip is attached to the device by using a layer of the PDMS mixture as adhesive and put into an oven for 45 minutes. Afterwards, the ends of the microstrip are bent down as they reach the bottom plate and SMA ports are soldered to the ends of the microstrip. The bottom plate is grounded to the SMA ports. Lastly, microfluidic ports are placed and sealed with epoxy. Media used for both cells were very similar in composition. The medium for HeLa cells is composed of DMEM (low glucose without L-glutamine), 10% FBS, 1% L-glutamine and 0.5% pen/strep antibiotic. The medium for MDA-MB-157 cells is composed of DMEM (low glucose without L-glutamine), 10% FBS, 1% NEAA and 1% pen/strep. No significant differences were observed in the resonance frequency of the sensors between the electrical responses of these media.

### Monte Carlo simulations for geometric size and effective permittivity

For the Monte Carlo simulations in MATLAB, an ensemble of 100 particles is generated with different position, size and electrical volume values. Since the ratio of electrical volume to the geometric size defines an effective electrical permittivity, the particles also differ in terms of permittivity which is recovered by the inertial imaging technique. The position for each particle was randomly assigned to be between 0.20 and 0.45 of the device length. The (geometric) size of each particle was randomly assigned between  $3.46 \times 10^{-3}$  and  $3.46 \times 10^{-2}$  (*i.e.* the standard deviation for the distribution had a range between  $10^{-3}$  and  $10^{-2}$  of the device length). For electrical volume of the particle, a range of  $10^{-3}$  to  $10^{-2}$  was used.

For each particle, the frequency shifts in the first four ideal modes of a microstrip line was simulated in Matlab using eqn (1) of the main text. These simulated frequency shifts are then processed with the inertial imaging algorithm to recover the electrical volume, position and size of the particles. Two iterations are used and the resolution is increased by the adaptive fitting protocol. Mass error is calculated to be  $8 \times 10^{-9}$  reported as the rms of fractional mass error between calculated and actual values. Position error is  $1 \times 10^{-8}$  reported in terms of the fraction of the microstrip line length. Such small error values are expected due to the adaptive fitting procedure which dramatically reduces fitting errors as the measurement zone is shrunk iteratively. Also, the frequency noise effects, which degrade any real measurement, are avoided in the simulated frequency shifts. The size in standard deviation is  $2 \times 10^{-3}$  again reported as the fraction of the microstrip line length. The effective permittivity of each particle is calculated by dividing the calculated values for the electrical volume to the size of each particle.

## Conclusions

We showed how multimode sensing techniques, originating from the mechanical domain, can be tailored for the electromagnetic domain by designing a suitable test platform, performing simulations, and conducting two-mode, frequency-shift experiments with a microfluidic device. Unlike capacitance-based sensing, where multiple capacitive electrodes must be fabricated and characterized, the proposed technique only uses a single electrode by multiplexing the electronic frequencies. As previously demonstrated, the resolution of the main approach (inertial imaging) is not limited by the wavelength of the resonance mode that is used (because this is not a far-field technique). However, it is limited by the signal-to-noise ratio of the frequency shifts.<sup>20</sup> Indeed, the two modes used in our experiments have wavelengths of 138 mm and 69 mm. So applying the Abbe limit, one can expect at best 34.5 mm of spatial resolution for far-field imaging. However, as shown in the Noise analysis section, we can achieve a sub-wavelength limit of 1.19 mm with our technique which is almost one-and-a-half order-of-magnitude smaller than the far-field limit. And the expected theoretical resolution (0.77 mm) from the frequency noise agrees with the observed resolution.

Detailed information about the spatial properties of analytes, such as their position, size, and skewness, can be obtained using higher-order electromagnetic modes. After these spatial parameters have been obtained, they can be used to reconstruct the image of an analyte passing through a microfluidic channel. In this method, images are constructed from the global image features (such as geometric moments or Zernike moments) rather than local information represented as pixels.

Imaging cells using the multimode technique provides two other remarkable advantages. First, image features (such as geometrical or Zernike moments) can be calculated with

minimal processing of data; in contrast, significant computational power is required to extract them from pixelated images. Second, the difference in the contrast between biological materials and the surrounding water is very large at the microwave band (the relative permittivity of proteins vs. water is 4–6 vs. 80 near 1 GHz); however, at optical frequencies, the indices of refraction for biological material and water are almost identical, resulting in lower inherent contrast. In addition, multimode resonant sensors have the potential to characterize both the morphological and electrical properties of individual cells simultaneously. This multidimensional aspect of the sensors can provide significant benefits for certain applications, such as the early detection of cancer, since cancer cells are known to differ from their normal counterparts both in terms of their morphological and dielectric properties.

With multimode microwave sensors, size and transit-time measurements can be conducted to gauge the mechanical properties of living cells, e.g., the determination of single-cell growth rates<sup>40</sup> or the detection of circulating tumor cells (CTCs). Also, the permittivity of the particles can be determined by combining the electrical volume and morphology measurements, providing an accurate means of identifying the composition of analytes. By using resonators that extend along two- and three-dimensions, images with higher dimensionality can be obtained. The technique proposed in this paper can be likened to a radar. Although the operation principles are different (reflection from an object vs. resonance frequency change due to an object), the utilities they offer are quite similar: ranging, sizing, locating, imaging and ultimately classifying objects of interest using microwaves without any labeling.

## Conflicts of interest

There are no conflicts to declare.

## Acknowledgements

MSH thanks B. Çetin for formative discussions on microfluidic sensing and for pointing out the potential of this field. MSH also thanks J. Sader and M. Roukes for discussions on inertial imaging techniques. We thank U. Seker, E. Duman, E. Kehribar, O. Akbulut, and M. Yavuz for providing us with HeLa and MDA cells. We also thank A. Atalar and S. Kasırga for lending some of the microwave components used in the experiments. We acknowledge the help of Ç. Karakan, A. Arı, E. Özelçi, U. Çalışkan, A. Nikdoost, Y. Erdem, R. Tarık, C. Yanık and İ. Kaya.

## References

- 1 G. M. Whitesides, *Nature*, 2006, **442**, 368–373.
- 2 T. M. Squires and S. R. Quake, *Rev. Mod. Phys.*, 2005, **77**, 977.
- 3 C. Zhang, D. Xing and Y. Li, *Biotechnol. Adv.*, 2007, **25**, 483–514.

- 4 S.-Y. Teh, R. Lin, L.-H. Hung and A. P. Lee, *Lab Chip*, 2008, **8**, 198–220.
- 5 H. Becker, *Lab Chip*, 2009, **9**, 1659–1660.
- 6 P. M. Valencia, O. C. Farokhzad, R. Karnik and R. Langer, *Nat. Nanotechnol.*, 2012, **7**, 623–629.
- 7 Z. Göröcs and A. Ozcan, *IEEE Rev. Biomed. Eng.*, 2013, **6**, 29–46.
- 8 K. Grenier, D. Dubuc, T. Chen, F. Artis, T. Chretiennot, M. Poupot and J.-J. Fournie, *IEEE Trans. Microwave Theory Tech.*, 2013, **61**, 2023–2030.
- 9 M. I. Mohammed, S. Haswell and I. Gibson, *Procedia Technol.*, 2015, **20**, 54–59.
- 10 J.-L. Fraikin, T. Teesalu, C. M. McKenney, E. Ruoslahti and A. N. Cleland, *Nat. Nanotechnol.*, 2011, **6**, 308–313.
- 11 R. Liu, N. Wang, F. Kamili and A. F. Sarioglu, *Lab Chip*, 2016, **16**, 1350–1357.
- 12 C. Laborde, F. Pittino, H. Verhoeven, S. Lemay, L. Selmi, M. Jongasma and F. Widdershoven, *Nat. Nanotechnol.*, 2015, 791–795.
- 13 M. Nikolic-Jaric, S. Romanuik, G. Ferrier, G. Bridges, M. Butler, K. Sunley, D. Thomson and M. Freeman, *Biomicrofluidics*, 2009, **3**, 034103.
- 14 G. Yesiloz, M. S. Boybay and C. L. Ren, *Lab Chip*, 2015, **15**, 4008–4019.
- 15 S. Dohn, W. Svendsen, A. Boisen and O. Hansen, *Rev. Sci. Instrum.*, 2007, **78**, 103303.
- 16 M. S. Hanay, S. Kelber, A. K. Naik, D. Chi, S. Hentz, E. C. Bullard, E. Colinet, L. Duraffourg and M. L. Roukes, *Nat. Nanotechnol.*, 2012, **7**, 602–608.
- 17 E. Gil-Santos, D. Ramos, J. Martinez, M. Fernandez-Regulez, R. Garcia, A. San Paulo, M. Calleja and J. Tamayo, *Nat. Nanotechnol.*, 2010, **5**, 641–645.
- 18 E. Sage, A. Brenac, T. Alava, R. Morel, C. Dupré, M. S. Hanay, M. L. Roukes, L. Duraffourg, C. Masselon and S. Hentz, *Nat. Commun.*, 2015, **6**, 6482.
- 19 S. Olcum, N. Cermak, S. C. Wasserman and S. R. Manalis, *Nat. Commun.*, 2015, **6**, 7070.
- 20 M. S. Hanay, S. I. Kelber, C. D. O'Connell, P. Mulvaney, J. E. Sader and M. L. Roukes, *Nat. Nanotechnol.*, 2015, **10**, 339–344.
- 21 Z. Pincus and J. Theriot, *J. Microsc.*, 2007, **227**, 140–156.
- 22 E. Alizadeh, S. M. Lyons, J. M. Castle and A. Prasad, *Integr. Biol.*, 2016, **8**, 1183–1193.
- 23 M. R. Teague, *J. Opt. Soc. Am.*, 1980, **70**, 920–930.
- 24 D. J. Rowe, S. Al-Malki, A. A. Abduljabar, A. Porch, D. A. Barrow and C. J. Allender, *IEEE Trans. Microwave Theory Tech.*, 2014, **62**, 689–699.
- 25 H.-J. Lee, J.-H. Lee and H.-I. Jung, *Appl. Phys. Lett.*, 2011, **99**, 163703.
- 26 A. Ebrahimi, W. Withayachumnankul, S. F. Al-Sarawi and D. Abbott, Microwave microfluidic sensor for determination of glucose concentration in water, *IEEE 15th Mediterranean Microwave Symposium (MMS)*, 2015.
- 27 A. Landoulsi, C. Dalmay, A. Bessaoudou, P. Blondy and A. Pothier, A Microwave Sensor Dedicated to Dielectric Spectroscopy of nanoliter volumes of Liquids Medium and Flowing Particles, *IEEE Topical Conference on Biomedical Wireless Technologies, Networks, and Sensing Systems (BioWireless)*, 2015.
- 28 M. H. Zarifi, P. Shariaty, M. Abdolrazzaghi, Z. Hashisho and M. Daneshmand, *Sens. Actuators, B*, 2016, **234**, 332–337.
- 29 M. H. Zarifi, S. Farsinezhad, K. Shankar and M. Daneshmand, *IEEE Microw. Wirel. Compon. Lett.*, 2015, **25**, 621–623.
- 30 M. H. Zarifi and M. Daneshmand, Non-contact Liquid Sensing Using High Resolution Microwave Microstrip Resonator, *IEEE MTT-S Int Microw Symp. Dig.*, May, 2015, pp. 1–4.
- 31 M. Abdolrazzaghi, M. H. Zarifi, M. Daneshmand and C. F. A. Floquet, Contactless Asphaltene Solid Particle Deposition Monitoring Using Active Microwave Resonators, *Ieee Sensors*, October, 2016, pp. 1–3.
- 32 S. Ingebrandt, *Nat. Nanotechnol.*, 2015, **10**, 734–735.
- 33 D. M. Pozar, *Microwave engineering*, John Wiley & Sons, 2009.
- 34 M. S. Boybay, A. Jiao, T. Glawdel and C. L. Ren, *Lab Chip*, 2013, **13**, 3840–3846.
- 35 K. D. Nyberg, M. B. Scott, S. L. Bruce, A. B. Gopinath, D. Bikos, T. G. Mason, J. W. Kim, H. S. Choi and A. C. Rowat, *Lab Chip*, 2016, 3330–3339.
- 36 D. Wong and C. L. Ren, *Lab Chip*, 2016, **16**, 3317–3329.
- 37 F. Hausdorff, *Math. Z.*, 1923, **16**, 220–248.
- 38 G. Athanassoulis and P. Gavriladis, *Probabilist. Eng. Mech.*, 2002, **17**, 273–291.
- 39 J. Skilling and R. Bryan, *Mon. Not. R. Astron. Soc.*, 1984, **211**, 111–124.
- 40 N. Cermak, *et al.*, High-throughput measurement of single-cell growth rates using serial microfluidic mass sensor arrays, *Nat. Biotechnol.*, 2016, **34**(10), 1052–1059.